


Article

The Replacement of Celestine (SrSO₄) by Strontianite (SrCO₃) in Aqueous Solution Studied In Situ and in Real Time Using Fluid-Cell Raman Spectroscopy

Michael Sulzbach ^{1,2,*} and Thorsten Geisler ¹ 

¹ Institute of Geosciences, Section Geochemistry/Petrology, University of Bonn, Meckenheimer Allee 169, 53115 Bonn, Germany; tgeisler@uni-bonn.de

² Federal Highway Research Institute (BASt), Section S1 Sustainable Road Construction and Road Maintenance, Bruederstraße 53, 51427 Bergisch Gladbach, Germany

* Correspondence: michael.sulzbach@yahoo.de

Abstract: The replacement of celestine (SrSO₄) by strontianite (SrCO₃) has extensively been studied over the past few decades. It also represents an ideal reaction to in situ study the kinetic and fundamental mechanistic details of mineral replacement reactions in aqueous solutions via fluid-cell Raman spectroscopy. This technique allows us to study the reaction process in real time by continuously analysing the solution or by imaging the solid–liquid interface where the reaction takes place and while the replacement process is ongoing. Two sets of experiments were conducted, the first of which was carried out with celestine powder and an equimolar Na₂CO₃ solution in a heated fluid cell between 30 and 60 °C. The progress of the reaction was followed by Raman spectroscopic in situ measurements of the solution. Another experiment was performed with a polished cuboid cut from a single celestine crystal and a 1 M Na₂CO₃ solution in a fluid cell at room temperature (21 °C). In this experiment, the reaction was studied in situ, spatially resolved, and in real time. The results of both types of experiments revealed that the replacement occurs via a coupled dissolution–precipitation mechanism and that the evolution of the solution composition cannot fully be explained by a single rate law derived from a shrinking core model. By applying the model-independent time-to-a-given-fraction method, three kinetic regimes could be identified and the associated activation energies quantified.

Keywords: celestine; strontianite; Raman spectroscopy; in situ; real time; fluid cell



Citation: Sulzbach, M.; Geisler, T. The Replacement of Celestine (SrSO₄) by Strontianite (SrCO₃) in Aqueous Solution Studied In Situ and in Real Time Using Fluid-Cell Raman Spectroscopy. *Minerals* **2024**, *14*, 164. <https://doi.org/10.3390/min14020164>

Academic Editor: Jordi Ibanez-Insa

Received: 22 December 2023

Revised: 24 January 2024

Accepted: 31 January 2024

Published: 2 February 2024



Copyright: © 2024 by the authors. Licensee MDPI, Basel, Switzerland. This article is an open access article distributed under the terms and conditions of the Creative Commons Attribution (CC BY) license (<https://creativecommons.org/licenses/by/4.0/>).

1. Introduction

Pseudomorphism is a wide-spread phenomenon in nature and involves the complete or partial replacement of one mineral by another or by the same mineral but with a different composition whereby the crystal shape of the parent mineral remains unchanged (e.g., [1]). The parent and the product phase can have the same or a different crystal structure. The partial replacement of one solid by another in aqueous solutions is also called alteration or corrosion, and there is still no general consensus about the replacement or alteration mechanism(s), e.g., [2–4]. The equilibration of minerals in the presence of an aqueous fluid phase has been described in terms of a number of potential mechanisms, particularly via diffusion-controlled solid-state ion exchanges between the solid and fluid phase or by interface-coupled dissolution–precipitation (ICDP) where equilibration is approached by the spatial and temporal coupling between the dissolution of the parent solid and the precipitation of a new solid along a moving reaction interface.

The replacement of celestine (Clt, SrSO₄) by strontianite (Str, SrCO₃), which both have the same orthorhombic crystal structure, in sodium carbonate-bearing aqueous solutions is observed in nature [1] but is also an important technical route to obtain strontium carbonate from the reaction of celestine with a Na₂CO₃ solution. Strontium carbonate is used, for instance, as an inexpensive colorant in fireworks, for strontium ferrite magnets,

for luminous paints, alloys, for electrolytes, medical uses like bone health products, and for the production of glass for colour television tubes (e.g., [5,6]). The replacement reaction in a carbonate-bearing solution can be represented by



The first experimental studies on this solid–aqueous solution reaction were already conducted in 1943 with natural celestine and Na_2CO_3 solutions by Kobe and Deiglmeier [7], followed by Busey and Pollard [8] and Booth and Pollard in 1948 [9]. However, none of these early studies investigated the thermodynamics, mechanisms, and kinetics of the reaction. It was not until 1989 when Iwai and Toguri [10] performed isothermal time-series experiments that it was found that the reaction kinetics could be divided into two kinetic regimes. These were mathematically described by a shrinking core model that was first invented by Wen in 1968 [11]. The first regime was attributed to a surface reaction-controlled process that was followed by a diffusion-controlled second regime, which yielded different activation energies of 71.5 and 64.1 kJ/mol, respectively. It was also shown that the concentration of sodium carbonate and the stirring speed of the solution had no direct impact on the reaction rate. The particle size, on the other hand, influences the reaction [12,13]. Based on the shrinking core model, Castillejos et al. [12] determined an activation energy of 70.05 kJ/mol, assuming a diffusion-controlled replacement process, which compares well with those determined by Iwai and Toguri [10]. On the other hand, Zoraga and Kahruman [14] reported an activation energy of 41.9 kJ/mol from experiments performed between 20 and 50 °C. Moreover, the results from hydrothermal experiments conducted at higher temperatures between 150 and 250 °C principally confirmed the shrinking core model with the diffusion of aqueous CO_3^{2-} ions through a porous strontianite product layer becoming rate-limiting with increasing reaction times [15,16]. However, this study yielded a much lower activation energy of 21.6 kJ/mol. It follows from the review of the literature that there is not yet a reliable quantitative understanding of the kinetics of the replacement process.

Here, we report the results of two different, novel in situ experimental studies on the mechanism and kinetics of the replacement reaction, both of which were designed and performed separately, but the results are worth discussing in a single contribution, because they complement each other. One set of experiments was carried out with celestine powder and an equimolar Na_2CO_3 solution in a heated home-made fluid cell between 30 and 60 °C for durations of up to 136 h to study the kinetics of the reaction. The progress of the reaction was followed by Raman spectroscopic in situ measurements of the solution (Figure 1a). The idea was to determine the kinetics of the reaction at a much higher time resolution than the typical time steps of hours used in conventional ex situ experiments, where a new sample–solution mixture must be heated and quenched for each time step before the solution and/or solid products can be analysed.

Another experiment was carried out at room temperature (21 °C) also in a home-made fluid cell with a 1M Na_2CO_3 solution and a polished cuboid cut from a single crystal of celestine. In this experiment, the reaction was studied in situ and spatially resolved by continuously mapping an area of $100 \times 45 \mu\text{m}^2$ to study the mechanistic details of the reaction as it proceeded (Figure 1b). The replacement of celestine by strontianite in aqueous solutions is an ideal reaction to in situ study the kinetic and fundamental mechanistic details of mineral replacement reactions in aqueous solutions via fluid-cell Raman spectroscopy [17]. This is because fluid-cell Raman spectroscopy allows us to study the replacement reaction in real time by continuously analysing the solution or, more sophisticatedly, by imaging the solid–liquid interface where the reaction takes place and while the replacement process is running. Using home-made heated fluid cells, our group has applied, for the first time, fluid-cell Raman spectroscopy to in situ study the corrosion of silica glasses in aqueous solutions with a spatial resolution of a few micrometres [17–20]. These experiments have given new, intriguing, and partly paradigm-breaking mechanistic insights in the glass corrosion process. Here, the replacement of celestine via the strontianite

reaction was chosen for an in situ Raman spectroscopic study because (1) both the parent and product phase are crystalline and transparent to visible light and have a simple crystal chemistry, (2) both oxo-anion species in the crystal as well as in the solution have relatively high Raman scattering cross sections, and (3) the reaction is already activated at room temperature. The celestine–strontianite replacement reaction is considered here as a model system to in situ study the mechanistic and kinetic details of mineral replacement processes via fluid-cell Raman spectroscopy, but it is also interesting in its own right due to the industrial importance of the reaction.

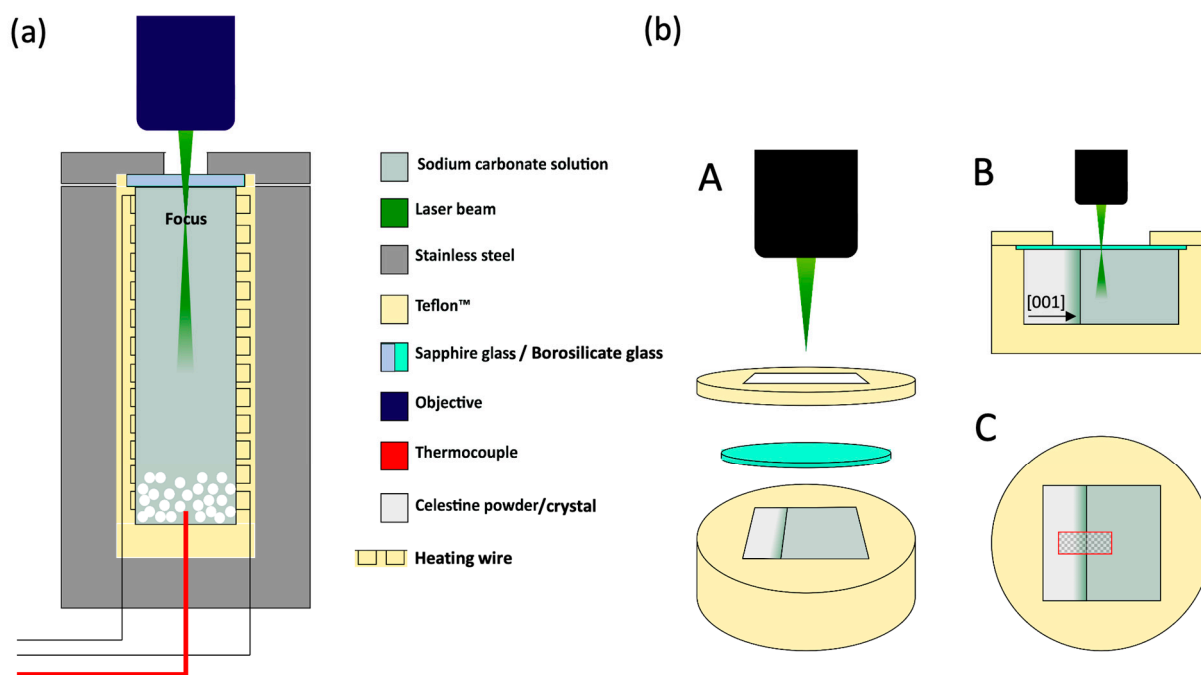


Figure 1. Schematic representation of the fluid cells used in both experimental approaches. (a) The fluid cell used for the powder and (b) for the single crystal experiment. The latter is shown from different perspectives (A–C). The red box in (C) indicates the imaging plane, including the initial interface between the celestine crystal and the solution. Not to scale.

2. Materials and Methods

2.1. Materials

Transparent, slightly blueish celestine crystals from Morocco were used for both types of experiments. The average chemical composition of the celestine crystals was determined via electron microprobe analysis using a JEOL 8200 Superprobe (JEOL Ltd., Akishima, Tokyo, Japan) at the Institute of Geosciences of the University of Bonn, Germany, equipped with a secondary and backscattered electron detector. A total of 200 spot analyses from polished sections, using a natural albite (Amelia), synthetic BaF_2 , strontianite (NMNH 10065, Smithsonian Institution, Washington, DC, USA), and FeS_2 (CAMECA, Gennevilliers Cedex, France) as standards for Na, Ba, Sr, and S, respectively, yielded an average composition of $(\text{Sr}_{0.973}\text{Ba}_{0.025}\text{Na}_{0.002})\text{SO}_4$. For the experiments, the crystals were washed with Milli-Q[®] (Merck KGaA, Darmstadt, Germany) water in an ultrasonic bath and dried for several hours at 60 °C in an oven. The crystals were then crushed, sieved to grain sizes between 0.063 and 0.125 mm, and washed again with Milli-Q[®] water. The specific surface area of the powder was determined via the Quantachrome GmbH (Anton Paar GmbH, Graz, Austria) using multi-point, krypton-based BET analysis, which yielded a value of $0.063 \pm 0.001 \text{ m}^2/\text{g}$.

For the single crystal experiment, a $2.5 \times 2.5 \times 8.0 \text{ mm}^3$ sized cuboid was cut from one larger crystal so that the longest edge of the cuboid was oriented parallel to the crystal's crys-

tallographic *c* axis (Figure 1b). For all experiments, a 1 M Na₂CO₃ solution was prepared from Milli-Q[®] water and 99.999% ultra-pure Na₂CO₃ (Sigma-Aldrich, St. Louis, MO, USA).

2.2. Experimental Setups

2.2.1. Powder Experiments

All powder experiments were conducted with a heated fluid cell made of Teflon[®] and stainless steel (Figure 1a). The cell was filled with 1.8195 ± 0.0003 mL of the prepared 1M Na₂CO₃ solution and an equimolar amount of the celestine powder, resulting in a specific surface-to-volume ratio of 1.1577 ± 0.0011 m⁻¹. The fluid cell was then immediately sealed with a 1 mm thick sapphire glass and placed on the automated x-y-z table of the Raman spectrometer. Experimental temperatures ranged from 30 to 60 °C in 5 °C steps, and run times varied between 65 and 97 h. Temperature measurements were accurate within ± 1 °C. After the termination of the experiment and cooling to room temperature, the reacted celestine powder and the solution were removed from the reactor, and the product phase was washed with Milli-Q[®] water, dried, and an aliquot was then mounted in epoxy resin and polished for Raman spectroscopic and backscattered electron (BSE) imaging via an electron microprobe.

2.2.2. Single Crystal Experiment

The single crystal experiment was carried out with the polished celestine cuboid and 0.3964 ± 0.0002 mL of the 1 M Na₂CO₃ solution in a simply designed fluid cell (Figure 1b). The geometrical surface-to-solution ratio was ~ 0.011 m⁻¹. After filling the fluid cell with the solution, it was immediately sealed with a 170 ± 5 μm thin borosilicate glass plate (SCHOTT D263M) (SCHOTT AG, Mainz, Germany) and placed on the x-y-z table of the Raman microscope. Since the fluid cell cannot be heated, the experiment ran at room temperature, monitored to be 21.0 ± 0.5 °C (air-conditioned laboratory), for about 10 days and thus lasted significantly longer than the powder experiments.

2.3. Modelling of the pH Evolution during the Replacement Reaction

Since the replacement reaction has been shown to strongly depend on the solution pH (e.g., [12]), the pH values were modelled for different one-molar mixtures of sulphate and carbonate solutions using PHREEQC interactive version 3 [21]. Modelling was performed at all eight temperatures used in the experiments, and the specific ion interaction theory (SIT) database was chosen as this gives better results for highly saline solutions. A continuous exchange between the celestine and strontianite was modelled, and the calculated pH values were plotted as a function of the conversion fraction in Figure 2. In general, the lower the temperature, the higher the pH. However, the pH remained well above 10 at all experimental temperatures until a conversion fraction of 0.9 was reached and overall decreased by about 1 log unit (Figure 2).

For pH values above 10, bicarbonate, HCO₃⁻, is far less abundant than the carbonate ion. Its Raman cross section is also significantly lower than that of the carbonate ion. It is thus not surprising that the most intense ν(CO-H) band near 1016 cm⁻¹ at room temperature [22] was not observed in any of the Raman spectra taken in this work. Therefore, bicarbonate was not considered in the data analysis, but a minor influence on the determination of the reaction rates cannot be ruled out.

2.4. Raman Spectroscopy

All Raman analyses presented in this contribution were conducted with the Horiba LabRam HR 800 Raman spectrometer (HORIBA, Ltd., Kyoto, Japan) that is attached to an Olympus BX 41 microscope (Evident Corporation, Tokyo, Japan.) with a Märzhäuser motorized x-y-z stage. The Raman spectra were excited by a power-adjustable, 2 Watt Nd:YAG solid-state laser (532.09 nm). For all experiments, the laser output was set to 1 W, from which about 350 mW reached the surface of the fluid-cell window. The scattered light was recorded with an electron multiplier, charge-coupled device (EM-CCD) detector after

passing through a 500 μm confocal hole and a 100 μm spectrometer entrance slit and being dispersed by a spectrometer grating with 600 grooves/mm. A Ne lamp was positioned near the fluid cell and an intense Ne line, that should appear at 1707.06 cm^{-1} in the Raman spectrum for the 532.09 nm laser [23], was used to correct any spectrometer shift during the long-time experiments [24]. With these settings, the spectral resolution was about 3.5 cm^{-1} for the frequency range of interest as given by the full width at half maximum values of the recorded Ne lines.

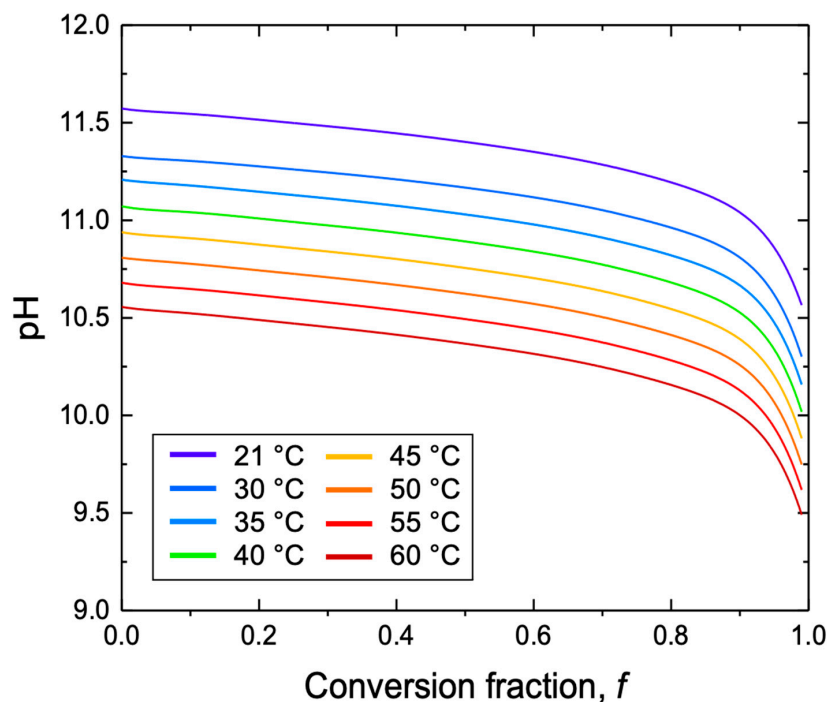


Figure 2. Modelled pH as a function of conversion fraction of celestine to strontianite for all eight experimental temperatures. Modelling was performed with the geochemical program PHREEQC using the SIT database [21].

2.4.1. Individual Analytical Settings for the Powder Experiments

For the powder experiments, Raman spectra were taken with a $50\times$ long working distance objective ($NA = 0.5$) and with the laser beam focussed 0.3 mm below the lower surface of the sapphire glass window into the solution. The confocal hole was fully opened (1 mm) as a high spatial resolution was not required. The first Raman map was recorded between 5 and 32 min after the cell had been filled with the solution and the desired temperature had been reached. The total acquisition time was 840 s, and the time steps were 900 s, i.e., significantly shorter than those for the single crystal experiment. The measurements were started once the desired temperature in the cell was reached. The maximum temperature of 60 °C, for instance, was reached in 5 min.

2.4.2. Individual Analytical Settings for the Single Crystal Experiment

For the single crystal experiment, a $100 \times 45\ \mu\text{m}^2$ sized area at a nominal depth of 180 μm below the glass window surface was selected and mapped with a $100\times$ long working distance objective (numerical aperture $NA = 0.8$) and a step size of 2 and 3 μm in the x and y directions, respectively. The total counting time per spectrum (pixel) was 5 s, which resulted in a total exposure time of ~ 2 h per image, including the point-to-point drive time.

In contrast to the powder experiment, in which only the bulk solution was analysed, knowledge of the spatial resolution is essential to correctly interpret the time-dependent hyperspectral Raman images from the single crystal experiment. The diffraction-limited

theoretical lateral and axial resolution at a polished surface is given as $1.22\lambda/\text{NA}$ and $4\lambda/(\text{NA})^2$. With $\lambda = 532$ nm and an objective with a NA of 0.8, the lateral and axial resolution close to the surface is in the order of 0.8 and 3.3 μm , respectively. However, the Raman effect has to be excited (and the scattered photons have to be collected) from regions that are located several tens to a hundred micrometres below the surface of the glass window after crossing multiple interfaces. Here, the axial resolution is estimated to be ten to a hundred times worse than the theoretical resolution given above mainly due to the refraction of the laser beam at the interfaces [25–27]. Thus far, a theoretical treatment for estimating the spatial resolution in multi-layered structures does not exist. We therefore empirically determined the lateral and axial resolution at the depth of Raman imaging from x-z profile measurements on a celestine cuboid in contact with MilliQ water in the fluid cell shown in Figure 1b. With a confocal hole size of 500 μm at an absolute depth of 306 μm below the surface of the glass window, the Raman signals were primarily collected from an approximately cylindrical volume with a diameter and height of about 4 and 32 μm , respectively. More details are given in Appendix A.

2.4.3. Data Evaluation

A Raman spectrum evaluation and a least-squares spectrum fitting were performed with the Horiba Scientific *LabSpec6* software (HORIBA, Ltd., Kyoto, Japan), whereas the data analysis program *OriginPro9* (OriginLab Corporation, Northampton, MA, USA) was used for all other data evaluations. As the first step, each spectrum was corrected for any spectrometer shift by fitting the Ne line at 1707.06 cm^{-1} with a Gauss function and shifting the spectrum by the difference between the observed and known frequency. The Raman spectra were then analysed in the frequency range between 900 and 1200 cm^{-1} , covering the energy range of the four fully symmetric stretching (ν_1) modes of aqueous and solid SO_4^{2-} and CO_3^{2-} groups at about 980, 1000, 1066, and 1072 cm^{-1} [28,29]. As expected, Raman spectra from the powder experiments show only the $\nu_1(\text{CO}_3)$ and $\nu_1(\text{SO}_4)$ bands of the aqueous phase near 980 and 1066 cm^{-1} , respectively (Figure 3a). The situation is different for the single crystal experiment. Here, due to the limitations of the spatial resolution, areas close to the celestine–strontianite–solution interfaces show all four bands (Figure 3b).

The integrated intensities, A , of the ν_1 bands were determined via a least-squares fitting of Gauss–Lorentz functions along with a linear background to the experimental band profiles. In the case of the single crystal experiment, the spatial distribution of the individual phases at each time step was visualised as false-colour hyperspectral Raman images from the integrated intensities of the ν_1 bands.

To convert the Raman intensity ratio between the $\nu_1(\text{CO}_3)$ and $\nu_1(\text{SO}_4)$ band of the aqueous phase, $A_{\text{S/C}}^{\text{aq}} = A[\nu_1(\text{SO}_4^{\text{aq}})] / A[\nu_1(\text{CO}_3^{\text{aq}})]$, into the molar ratio, $R^{\text{aq}} = [\text{SO}_4^{\text{aq}}] / [\text{CO}_3^{\text{aq}}]$, we prepared solutions from Na_2CO_3 and Na_2SO_4 with known molar ratios, recorded a Raman spectrum at room temperature, and determined $A_{\text{S/C}}$ from the Raman spectrum. In Figure 4, we have plotted the known molar R^{aq} ratio against $A_{\text{S/C}}^{\text{aq}}$ and fitted a calibration line to the data. The R^{aq} of the solutions was then obtained by multiplying the measured intensity ratio with the slope of the calibration line, i.e., with 0.4668 ± 0.0029 . From the molar ratio, we also calculated the molar conversion fraction of celestine to strontianite, f , from

$$f = R^{\text{aq}} / (R^{\text{aq}} + 1) \quad (2)$$

As a relative measure of celestine conversion or strontianite formation in the single crystal experiment, we determined the ratio of the integrated intensities of the $\nu_1(\text{CO}_3)$ band of strontianite and celestine, $A_{\text{S/C}}^{\text{Solid}} = A[\nu_1(\text{CO}_3^{\text{Str}})] / A[\nu_1(\text{SO}_4^{\text{Clt}})]$, from the average spectrum of each time step ($n = 816$ single spectra per map). To be more quantitative, we estimated the relative Raman band cross section between the ν_1 band of the CO_3 and

SO₄ groups in strontianite and celestine, respectively, at room temperature from Raman measurements of randomly oriented celestine grains were partly been replaced by strontianite. From pure single-phase spectra, we obtained an average value of 0.47 ± 0.05 (Figure 2). This value was then used to convert the intensity ratio into an apparent molar ratio between strontianite and celestine, $R^s = A_{S/C}^{Solid} 0.47u$, with $u = 1.177$ being the conversion factor for converting volume in mole fractions assuming densities of 3.975 and 3.760 g/cm³ for celestine and strontianite, respectively. Note that (1) the size of the selected celestine area from the Raman images was chosen arbitrarily, so that the determined absolute fraction of strontianite is not comparable to the fraction determined from the solution data, and (2) the ratios R^{aq} and R^s were defined to be positively correlated with the progress of the replacement reaction.

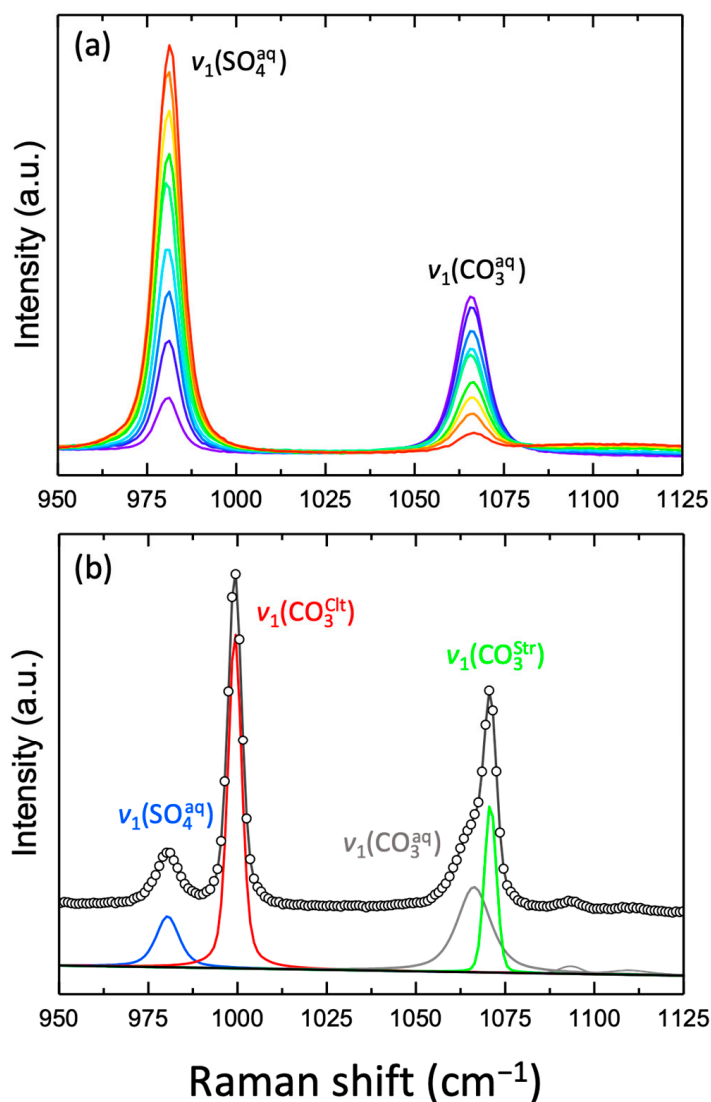


Figure 3. Representative Raman spectra from (a) solutions with a different molar $[\text{CO}_3^{2-}]/[\text{SO}_4^{2-}]$ ratios used for calibration (red: 10 mol.% CO_3^{2-} and 90 mol.% SO_4^{2-} → purple: 90 mol.% CO_3^{2-} and 10 mol.% SO_4^{2-}) and (b) the strontianite layer formed during the single crystal experiment, showing all four ν_1 bands along with the least-squares fit of Gauss–Lorentz functions to the four bands and two very weak and broad signals near 1094 cm^{-1} and 1112 cm^{-1} . The fitted Gauss–Lorentz functions and the linear background are shifted for clarity, whereas the sum spectrum is shown directly below the data.

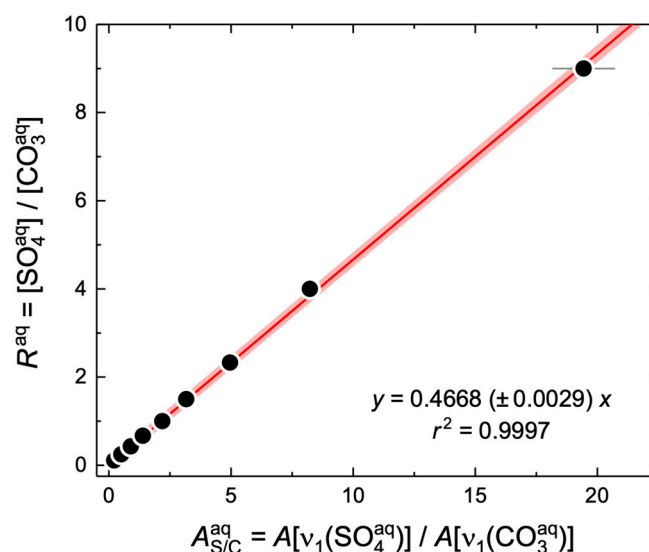


Figure 4. The molar ratio, R^{aq} , of synthetic solutions as a function of the measured Raman intensity ratio, $A^{\text{aq}}_{\text{S/C}}$. The red line represents a linear fit to the data that was anchored at the origin and is shown along with its 95% confidence bands.

3. Results

3.1. Powder Experiments

3.1.1. Ex Situ Textural Observations

Previous ex situ experiments with individual celestine crystals or aggregates in Teflon-lined autoclaves showed that the morphology of the crystals does not change during displacement by strontianite [8–10], but that the originally transparent, bluish celestine crystals become opaque and white (Figure 5a). Since strontianite crystals are transparent to translucent, the white colour must stem from light scattering along pores in the new strontianite, the sizes of which must be in the range of the wavelength of visible light. Moreover, it is also remarkable that the morphology of the original celestine crystal is very well retained, an observation that is a typical feature of pseudomorphs.

To investigate the textural relationship between the strontianite product and celestine parent phase, we analysed the celestine powders recovered at the end of the experiments using backscattered electron (BSE) and Raman imaging. Figure 5b–d show representative BSE images of the product powder from the 35, 45, and 55 °C experiments. In Figure 5e, a Raman image of a single grain, containing an unreacted celestine core surrounded by a strontianite rim with a gap between both phases, is shown. Such a characteristic gap between the celestine core and the strontianite rim is also observable in many other grains (yellow arrow in Figure 5c). It is noteworthy that a relic of such a gap can still be observed in those grains that are fully replaced by strontianite (blue arrow in Figure 5b,d).

3.1.2. Kinetic Analysis

Figure 6 summarizes the results from a kinetic analysis of the powder data. Figure 6a shows the progression of the conversion f as a function of time (and of the square root of time in the inset) for all seven powder experiments and the single crystal experiment at 21 °C. Although the surface-to-volume ratios of the powder and single crystal experiments are different, so they are not strictly comparable, we have plotted the solution data of the single crystal and the powder experiments together, as they nevertheless show similar kinetics and follow systematic trends. Already at the first glance, it is discernible that the isothermal trends cannot be described by a single rate law over the entire time and temperature range. This is also well discernible in the plot of f against the square root of time (inset in Figure 6a). At 21 and 30 °C, a sudden increase in f can be observed after a reaction time of about 6.4 and 14 h, respectively, clearly marking a change in the reaction kinetics.

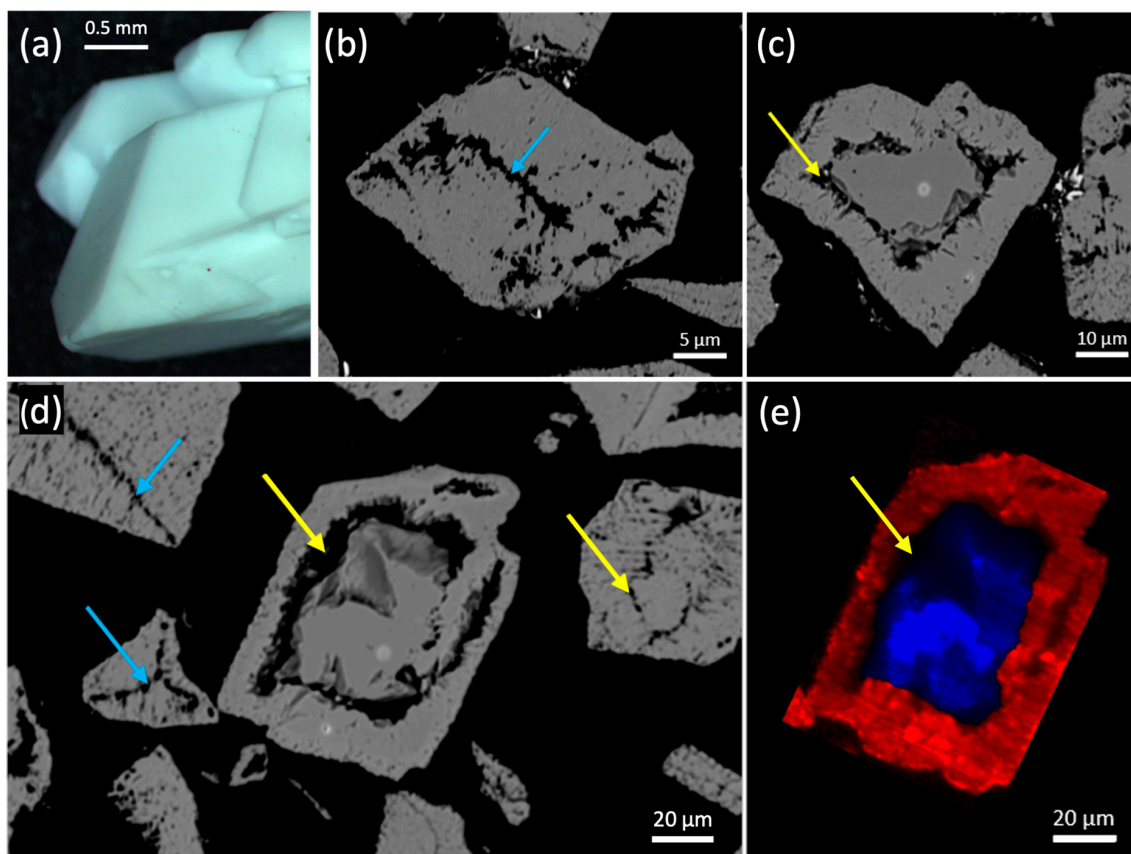


Figure 5. (a) Optical image of a celestine crystal aggregate after it has been completely replaced by strontianite in a sodium carbonate solution at 90 °C for 16 days (unpublished results from preliminary experiments). Note the white colour and the retained crystal morphology. (b–d) Backscattered electron images from reacted celestine grains from (b) the 35 °C, (c) the 45 °C, and (d) the 55 °C powder experiments. (e) A colour-coded hyperspectral Raman image from the grain in the centre of the image shown in (c). Strontianite is shown in red and celestine in blue. Note the formation of a gap between celestine and the strontianite layer (yellow arrows), a relic of which is still visible in those grains that were fully replaced by strontianite (blue arrows).

Previous *ex situ* experimental results from powder experiments were analysed within the framework of an unreacted shrinking core model for spherical and mono-sized particles [11]. This model considers that the replacement of celestine by strontianite is isovolumetric and the transport of reactants and products through the growing strontianite is rate limiting. For the special case where stoichiometric amounts of celestine and Na_2CO_3 reacted, as in this study, Castillejos and co-workers [12] derived the following rate law where k_p is a parabolic rate constant and t is the reaction time:

$$k_p t = \ln(1 - f) - 3(1 - (1 - f)^{-1/3}) \quad (3)$$

In Figure 6b, we have plotted $\ln(1 - f) - 3(1 - (1 - f)^{-1/3})$ as a function of time. If the data fulfil the requirements of the model, the data should define a linear trend with an intercept through the origin. However, this is evidently not the case for all temperatures except for 60 °C, where the data can be well described by a linear function over the entire duration of the experiment ($r^2 = 0.99783$). For the other temperatures, the data are visibly curved, showing that they do not fully comply with the rate law of Equation (3). We nevertheless have fit the data with a linear function to obtain the parabolic rate constants k_p that should yield at least an estimate of the activation energy for the diffusion-controlled regime of the replacement process. For this, we plot the data in an Arrhenius diagram,

i.e., the logarithms of the rate constants as a function of the reciprocal temperature, T , where they define a linear trend with a slope that corresponds to an activation energy of 22.8 ± 1.2 kJ/mol (Figure 7a).

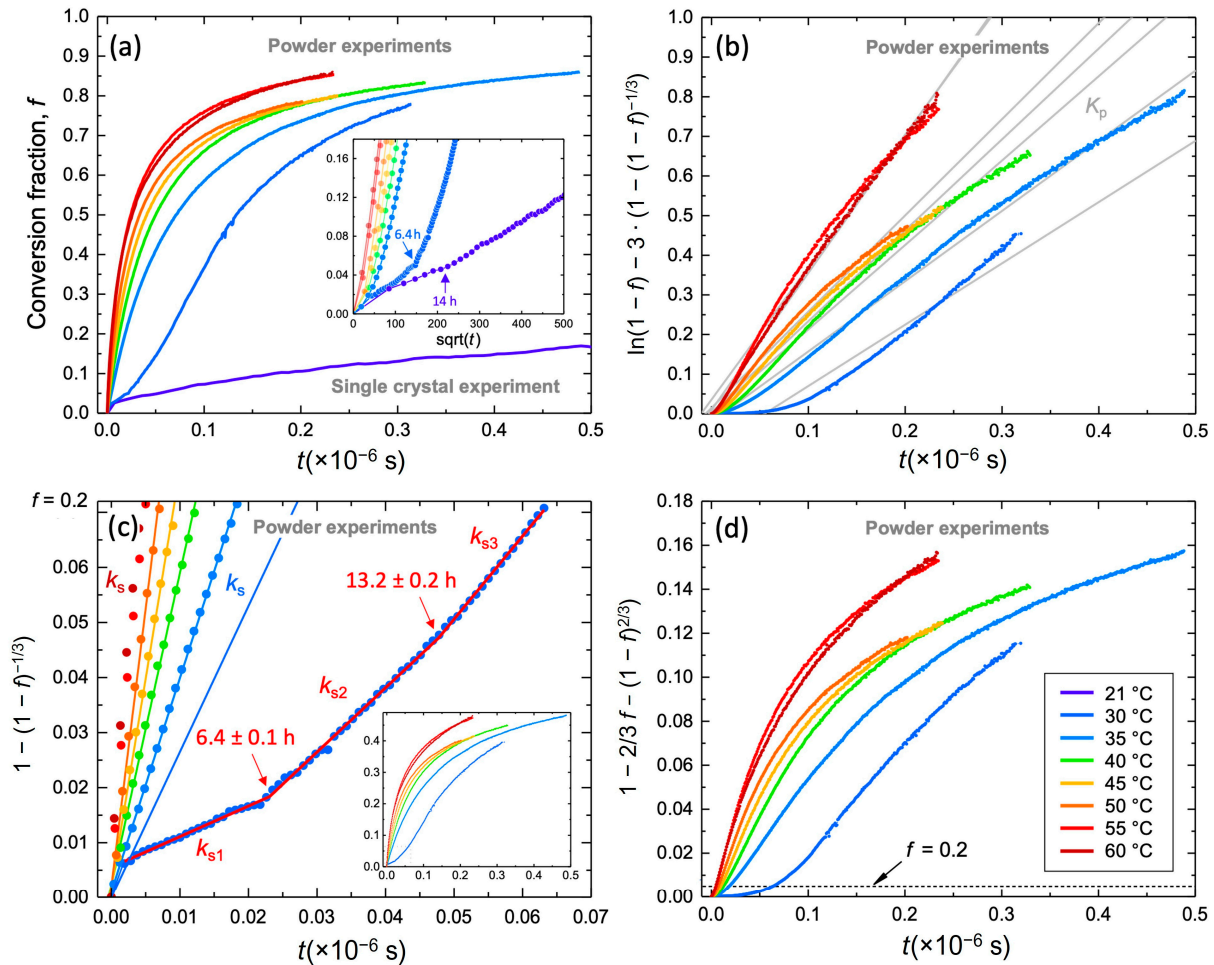


Figure 6. Plots of (a) conversion rate, f , (b) $\ln(1 - f) - 3(1 - f)^{-1/3}$, (c) $1 - (1 - f)^{1/3}$, and (d) $1 - 2/3f - (1 - f)^{2/3}$ as a function of time (and square root of time in the inset of (a)) for all powder experiments and in (a) additionally for the solution data of the single crystal experiment performed at 21 °C.

We further applied the kinetic analysis of Iwai and Toguri [10], who also considered an unreacted shrinking core model, but individually distinguished two rate-limiting regimes for the replacement reaction. In the initial regime, i.e., until 20% conversion ($f < 0.2$), the reaction was found to be surface-controlled, whereas at a higher degree of conversion ($f > 0.2$), their data could be well described by a rate law that is based on the diffusion-control of reactants and products through the strontianite layer. In the initial surface-controlled regime, the rate equation is

$$1 - (1 - f)^{1/3} = k_s t \tag{4}$$

with k_s as the rate constant for the surface-controlled initial regime, whereas the rate law for the diffusion-controlled kinetic regime, k_d , is given as

$$1 - 2/3f - (1 - f)^{2/3} = k_d t \tag{5}$$

Here, k_d includes the effective diffusion coefficient of reactants and products through the growing strontianite layer. In Figure 6c,d we have plotted $1 - (1 - f)^{1/3}$ and $1 - 2/3f -$

$(1 - f)^{2/3}$, respectively, as a function of time. The data with $f < 0.2$ and $T \geq 35^\circ$ can indeed be well fitted by a linear function when plotted as $1 - (1 - f)^{1/3}$ versus time (Figure 6c). At 30°C , however, data with $f < 0.2$ rather define three linear trends with kinks at 6.4 ± 0.1 and 131.1 ± 0.2 h. We therefore fitted the data with a piecewise linear function to obtain the rate constants k_{s1} , k_{s2} , and k_{s3} from the three linear sections. The first linear section with rate constant k_{s1} did not intersect the origin, because in the first 4 h, the reaction was faster, i.e., at 30°C the first kinetic step was not (fully) linear with $1 - (1 - f)^{1/3}$. The initial rate was therefore estimated by fitting a line through the origin and the first two data points. Interestingly, the logarithm of the slope (rate constant k_s) of this line plot in the Arrhenius diagram on the linear trend was defined by all other data, which corresponded to an activation energy of 52.5 ± 1.5 kJ/mol. The three rate constants k_{s1} , k_{s2} , and k_{s3} of the 30°C experiment, however, clearly plotted significantly away from this trend (Figure 7a). The slope of a linear function between the 35°C and 30°C (k_{s2}) data point corresponded to a high apparent activation energy of about 210 kJ/mol. Note that the data with $f > 0.2$ clearly did not define a linear trend when plotted as $1 - 2/3f - (1 - f)^{2/3}$ over time.

Since none of the rate laws describes the data well, we also applied the time-to-a-given-fraction method, which is independent of the assumption of a rate law and allows us to study the activation energy as a function of the reaction progress (e.g., [2,3]), here given as R^{aq} . For this, we determined the time needed to reach a given R^{aq} value, $t_{R^{\text{aq}}}$, at each temperature by linearly extrapolating between data points. The logarithm of $t_{R^{\text{aq}}}$ was then plotted against $1/T$ to obtain an empirical activation energy, E_A , for the replacement reaction for each $t_{R^{\text{aq}}}$ value from the slope of an Arrhenius-type relationship between $-\ln(t_{R^{\text{aq}}})$ and $1/T$ (Figure 7b), which is given as

$$-\ln(t_{R^{\text{aq}}}) = \ln(a) - \frac{E_A}{R} \cdot \frac{1}{T} \quad (6)$$

where R is the gas constant and a is the pre-exponential factor. Again, the data from the 30°C experiment plotted away from the linear trend defined by the other data in the Arrhenius diagram. We thus fitted a piecewise linear function with two linear sections to the data. From the two slopes, we calculated the activation energies (Figure 7b). Note that we also included three $t_{R^{\text{aq}}}$ values from the single crystal experiment at 21°C in this diagram. It is noteworthy that they were plotted close to the linear predictions resulting from the least-squares fits to the low-temperature linear section (dotted lines in Figure 7b), despite the different surface-to-volume ratio and geometrical constraints in both experiments. This observation is an indication that the change in the slope in the Arrhenius diagram, which is only defined by the 30°C data point, is actually real.

In Figure 7c, we have plotted the empirical activation energies obtained from the slopes of the two linear sections as a function of R^{aq} . Two trends can clearly be distinguished ($<35^\circ\text{C}$ and $35\text{--}60^\circ\text{C}$), and both can be well fitted with an exponential decay function which takes the following form:

$$E_A = E_A^\infty + A \cdot \exp(-R^{\text{aq}}/\lambda) \quad (7)$$

where λ is the decay constant. Here, E_A^∞ can be interpreted as the activation energy of the rate-limiting reaction at infinite conversion and the sum of E_A^∞ and A as the activation energy of the corresponding rate-limiting process at the beginning of the reaction, i.e., far away from equilibrium. From the least-squares fit of Equation (7) to the two trends, we obtained E_A^∞ of 37 ± 5 and 27.1 ± 0.9 kJ/mol. Both values should merge at infinite conversion. In the following, we therefore will only consider the more precise value from the higher temperature regime (Figure 7c). The empirical activation energies at zero conversion are 276 ± 11 and 71.8 ± 1.7 kJ/mol for the low- ($<35^\circ\text{C}$) and high-temperature ($\geq 35^\circ\text{C}$) regime, respectively. Hence, once more, there is evidence for a high activation energy for the initial reaction step. All activation energies determined in this study with the different methods are listed in Table 1 together with published values.

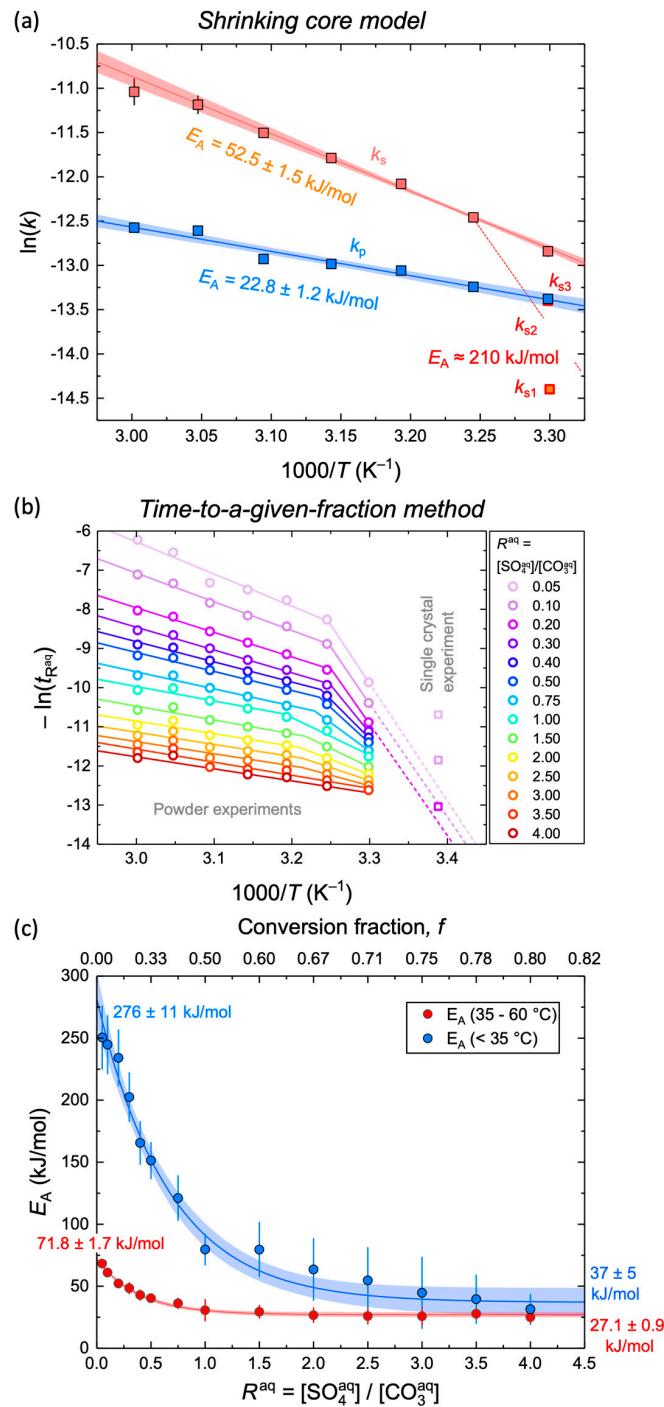


Figure 7. Kinetic analysis using rate constants obtained via shrinking core models and the time-to-a-give-fraction method. (a) Arrhenius diagram with rate constants, obtained via two different shrinking core models, with linear least-squares fitting lines and their 95% confidence bands. The rate constants k_p were obtained using the model of Castillejos et al. [12], shown in Figure 6a, whereas the rate constants k_s were determined following the kinetic analysis of Iwai and Toguri [10] as shown in Figure 6c. (b) The negative logarithm of the time required to reach a given molar ratio R^{aq} in solution as a function of $1/T$. Solid lines represent piecewise linear fits to the data and stippled lines represent their predictions towards lower temperatures. (c) The empirical activation energies, obtained via the time-to-a-give-fraction method, as a function of R^{aq} with exponential decay fits to the two trends (Equation (7)) and their 95% confidence bands. For more details, see text.

Table 1. Summary of experimental activation energies for the replacement of celestine by strontianite.

| Reference | A | B | C | D | This Study | |
|----------------|-----------------------|---------|-------|-------|---------------------------------|---|
| T (°C) | 25–55 | 150–250 | 25–75 | 20–50 | 30–60 | |
| Kinetic model | Shrinking core models | | | | Time-to-a-given-fraction method | Interpretation (rate-limiting step) |
| E_A (kJ/mol) | 71.5 | | 70.05 | | ~210 | Dissolution |
| | 64.1 | | | 41.9 | 52.5 ± 1.5 | ICDP |
| | | 21.6 | | | 22.8 ± 1.2 | <i>Meaningless?</i> |
| | | | | | 27.1 ± 0.9 | Transport (at high reaction progress) |

Abbreviations: ICDP: Interface-coupled dissolution–precipitation, A: Iwai and Toguri [10], B: Suárez-Orduña et al. [16], C: Castillejos et al. [12], D: Zoraga and Kahruman [14].

3.2. Single Crystal Experiment

3.2.1. In Situ Textural Observations

Figure 8 shows representative hyperspectral Raman images of the replacement of celestine (red) by strontianite (green) which were recorded in situ at different times while the reaction was in progress. It can be seen from the images that with increasing time, more and more strontianite replaced the celestine crystal along an uneven reaction front whereby the replacement reaction continuously slowed down. A contemporaneously increasing aqueous sulphate concentration is represented in the images by an increasing amount of the blue colour of the area occupied by the solution. At the end of the experiment, the strontianite rim within the imaged area reached a final thickness between ~10 and 15 μm .

3.2.2. Kinetic Analysis

A full quantitative kinetic analysis is not possible from a single isothermal experiment. Moreover, in the in situ experiment, the replacement reaction is followed only along the c axis, while in the powder experiments, the grains are replaced along all crystallographic orientations. However, a qualitative comparison with the powder data in a plot of the R^{aq} as a function of the square root of time reveals a systematic transition of the overall reaction rate from a low- (<35 °C) to a high- temperature (≥ 35 °C) regime (Figure 9a). Here, two characteristics are noticeable. First, the initial overall solution composition evolution was clearly not linear with the square root of time (1. kinetic regime), but became linear ($r^2 = 0.9963$) after about 14 h (2. kinetic regime), notably with a larger positive slope, i.e., with an increased reaction rate. It is recalled that a similar sudden increase in the reaction rate was also observed in the 30 °C powder experiment after 6.4 ± 0.1 h and after a similar conversion fraction of about 0.05 had been reached (Figure 6a). Second, R^{aq} increasingly fluctuated in waves around the overall linear trend as the reaction time increased. The oscillations were therefore significantly larger than the error of the measurements which was smaller than ± 1 –2%.

So far, information about the kinetics and underlying mechanisms of the replacement reaction has been obtained exclusively from the temporal evolution of the solution composition. However, the in situ Raman data from the single crystal experiment also provide solid-state information on the evolution of the replacement reaction. In Figure 9b, we plotted the molar ratio between celestine and the strontianite formed, R^{s} , against the square root of time. Again, wavy fluctuations can be observed around a linear trend that broke off after 131.3 ± 0.1 h, which was determined via a piecewise linear fit to the data assuming two linear sections. The kink after 131 h indicates a sudden slowdown in strontianite formation, i.e., another rate change into a new kinetic regime, while the chemical evolution of the solution remained unchanged (Figure 9a). We further plotted R^{aq} versus R^{s} (Figure 9c) and the ratio $R^{\text{aq}}/R^{\text{s}}$ as a function of time (Figure 9d). As expected, R^{aq} and R^{s} are well correlated, but the trend is distinctly non-linear. On the other hand, the two inflection points at about 14 and 131 h, that are observed in the plots of R^{aq} and R^{s} versus the square root of

time, respectively, and that clearly define three distinct kinetic regimes within the duration of the experiment (Figure 9a,b), are also well correlated with two inflection points that are observable in the plot of R^{aq} versus R^s (Figure 9c). The data between these two inflection points, i.e., within the second kinetic regime, define a linear trend with a slope of about 0.76. In the first and third kinetic regimes, the correlation between R^{aq} and R^s is rather curved. In the first regime, the strontianite formed is not associated with an equivalent increase in aqueous sulphate, while in the third regime, the situation is reversed. This is also noticeable in the plot of R^{aq}/R^s versus time (Figure 9d). The most important observation in this plot, however, is the occurrence of regular oscillations with a wavelength of 27 ± 4 h (Figure 9c). It is noted that we are dealing with intensity ratios and spectrometer shift-corrected data, so there is no obvious systematic analytical error that could explain the observed oscillation.

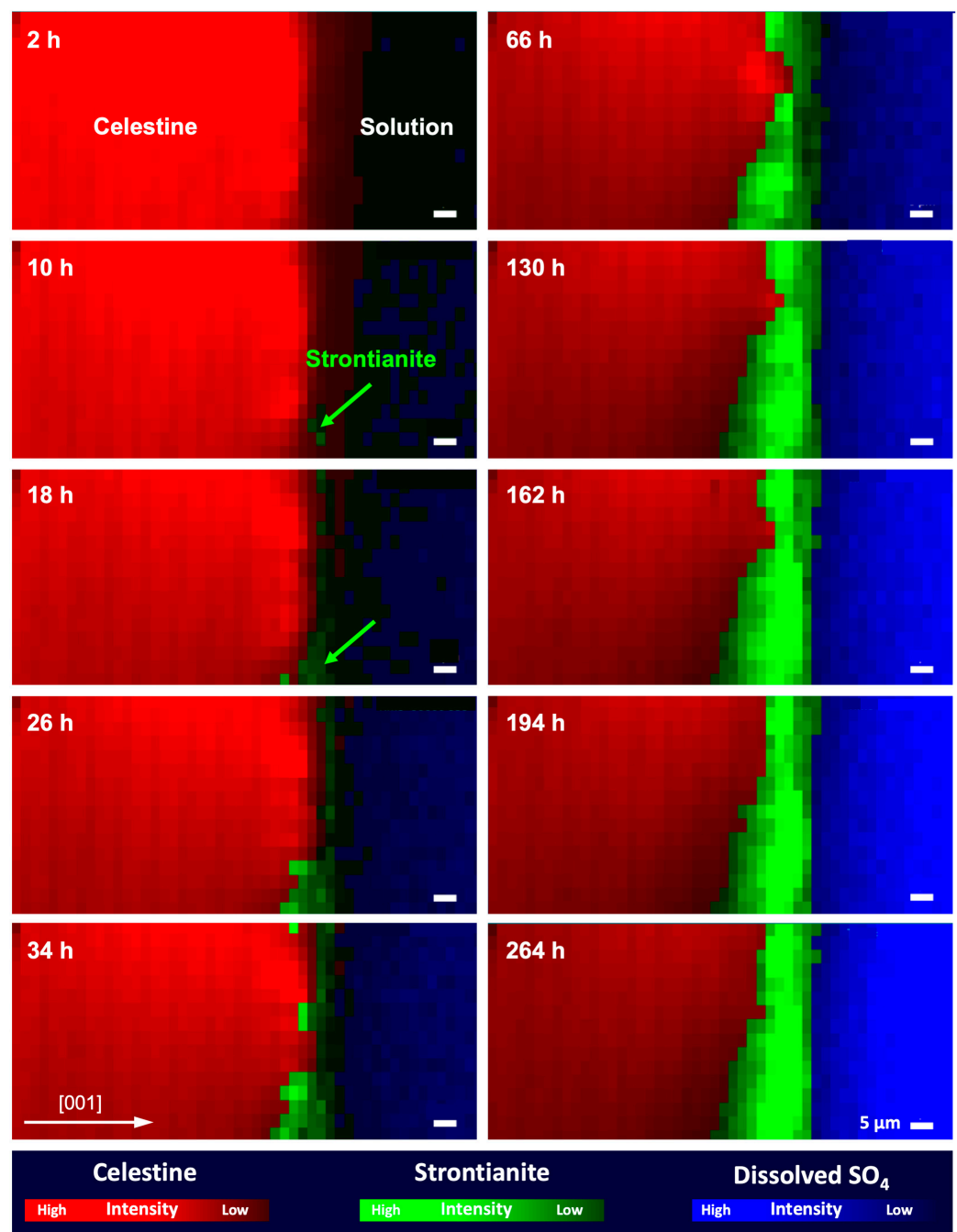


Figure 8. Representative hyperspectral Raman images from the in situ single crystal experiment taken at different reaction times.

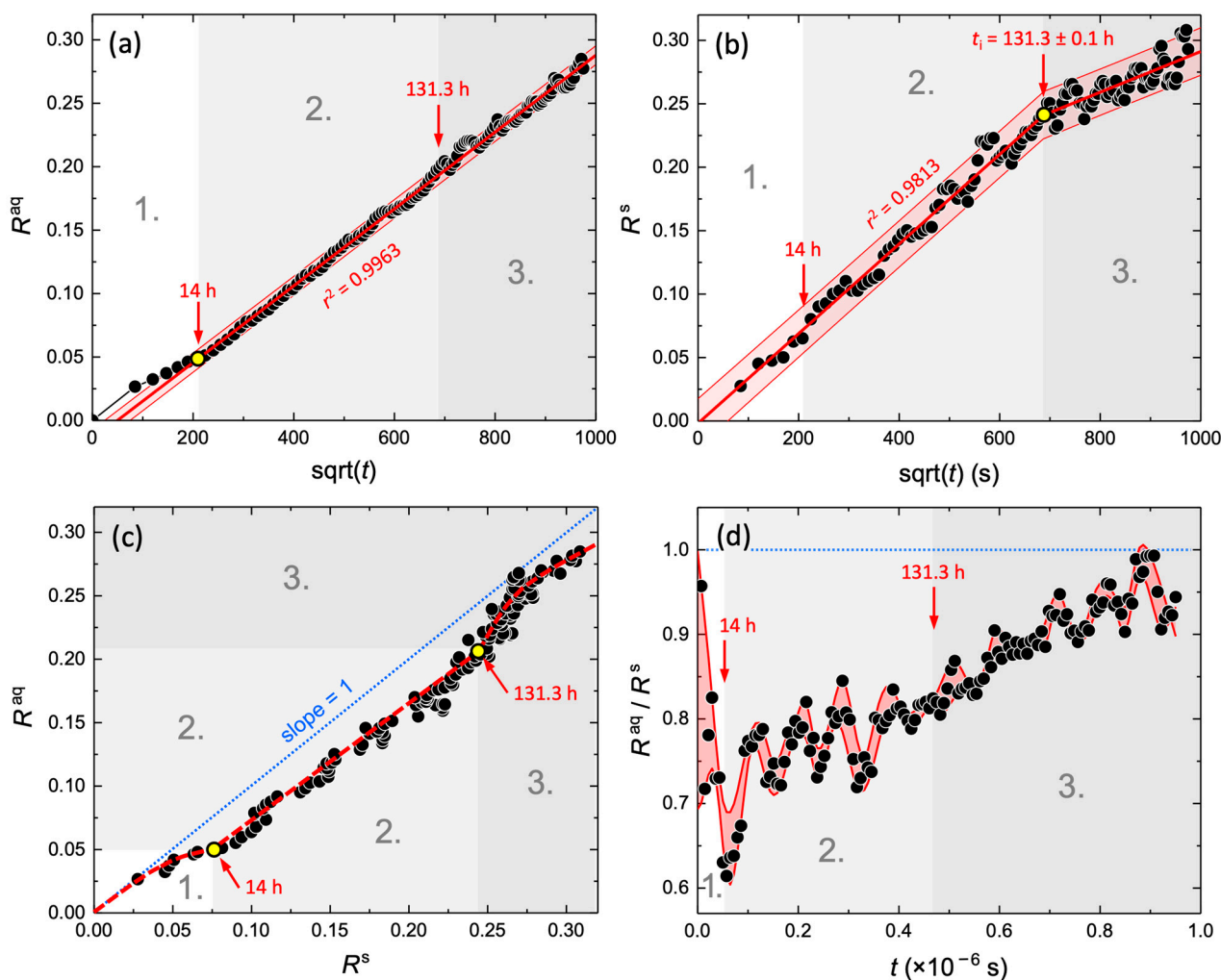


Figure 9. Kinetic analysis of the isothermal single crystal experiment. The three kinetic regimes are indicated by distinct inflection points that are marked by yellow circles in the diagrams. (a) R^{aq} versus the square root of time with a linear regression line through the data of the 2. and 3. kinetic regimes with its 95% prediction band. (b) R^s versus the square root of time with a piecewise linear regression through the two linear sections and the 95% prediction band. The intersection of the two linear segments defines a clear inflection in the reaction trend. (c) R^{aq} versus R^s with stippled red lines that are guides to the eye only. (d) R^{aq}/R^s as a function of time, showing regular oscillations. The red envelope following the oscillations was calculated by finding all points in the data whose first-order derivative is zero, through which a cubic spline interpolation was then performed. For more details, see text.

4. Discussion

In contrast to isochemical solid-state phase transformations, the re-equilibration reaction in the presence of a fluid phase moves from the solid–fluid interface into the solid phase (discontinuous reaction) and usually involves a change in composition. From the perspective of the solution composition, such reactions are often described as incongruent dissolution reactions. Incongruent dissolution has been interpreted to occur if different structural and chemical units of a mineral have different dissolution rates [30]. In a mechanistic context, incongruent dissolution was interpreted to occur as a result of a diffusion-controlled “leaching” process that operates in the solid state and may involve ion exchange, hydrolysis, hydration, electron transfer, and/or re-condensation reactions (e.g., [31–33]). The transformation of leucite to analcime [34], the formation of an amorphous silica-rich surface layer during feldspar dissolution (e.g., [33]), the alteration of

natural pyrochlore (e.g., [35]), or the oxidation of sulphides (e.g., [36]), for example, have been explained by a diffusion–reaction (“leaching”) process. However, it seems to be highly unlikely that the replacement of celestine by strontianite involves the (inter)diffusion of sulphate and carbonate anion units inside a stable Sr sublattice, leaving behind a porous strontianite layer. Putnis [2] has proposed that most, if not all, replacement reactions can be better explained by an interface-coupled dissolution–reprecipitation (ICDP) process. In this model, it is assumed that the congruent dissolution of the parent phase (here, celestine) is temporally and spatially coupled to the precipitation of a stable phase (here, strontianite) or phases at an inwardly moving reaction interface. The thermodynamic driving force for such a reaction is the solubility difference between the parent and product phase(s) or the free energy change that is associated with textural equilibration. The in situ and textural observations made in this study are fully consistent with such an ICDP process.

In a solution undersaturated with respect to the product phase(s), the parent phase will initially dissolve congruently (stoichiometrically) until a certain supersaturation of a product phase is reached in a surface solution boundary layer so the product phase(s) can topotaxially nucleate and grow on the retreating celestine surface [4], even though the bulk solution may still be undersaturated with respect to the product phase(s) [4,17,37], making the overall reaction incongruent. Solution saturation calculations with the geochemical program PHREEQC [21] showed that at 21 °C and in a 1M Na₂CO₃ solution, strontianite was already saturated after merely $\sim 2 \times 10^{-10}$ mol Sr atoms had entered the solution ($\approx 5 \times 10^{-7}$ mol/L). This concentration was already reached after a mere ~ 0.1 nm thick layer of celestine had dissolved into solution, i.e., strontianite very likely precipitated within the first minutes of the experiments from a highly supersaturated solution [38]. We assign the high apparent activation energies (~ 210 and 276 ± 11 kJ/mol) to this initial reaction step (Table 1), whereby the latter, derived from the model-independent time-to-a-given-fraction method, is regarded to be more reliable. However, while it is clear that there is a distinct kink in the Arrhenius diagram between 30 and 35 °C, such a high activation energy has not yet been reported (Table 1) and its accuracy is difficult to assess, since it is determined from only two data points (temperatures). Iwai and Toguri [10] assigned an apparent activation energy of 71.6 kJ/mol to the initial surface-controlled kinetic regime, which, in the framework of the ICDP and the mathematical shrinking core model, involves the initial dissolution of celestine and re-precipitation of strontianite before the strontianite layer increasingly becomes a diffusion barrier. However, in their experiments, the experimental time steps were 15 min plus heating and quenching time, and for each time step, a new powder sample had to be used. Thus, weak kinks in the conversion rate would probably not be resolvable in their dataset, even if they exist. Using their two-step model for the initial surface-controlled reaction step (Figure 6c), we obtained an apparent activation energy of 52.5 ± 1.5 kJ/mol from the 35 to 60 °C data (Figure 7a). This value is also comparable with an activation energy of 41.9 kJ/mol reported by Zoraga and Kahruman [14], but it is considered here to be meaningless, since the results of the model-independent time-to-a-given-fraction do not indicate such an activation energy (Table 1). We thus interpret these activation energies as being an undefined function of activation energies of all rate-limiting steps.

At the beginning of the reaction at 30 and 21 °C, the reaction rate slowed down until 6.4 and about 14 h, respectively, and then suddenly increased again, as indicated by clear kinks towards higher reaction rates (Figures 6 and 9). The initial slow-down of the reaction rate is likely related to an increasing surface cover with strontianite nuclei and a decreasing chemical affinity which is defined as the negative partial derivative of Gibbs free energy of the reaction with respect to the extent of reactions at a constant temperature and pressure. At a higher temperature, the initial kinetic regime proceeds so fast that it is not recognizable as an individual reaction step. Here, the conversion rate trends are also distinctly different to those at lower temperatures (Figure 6a). Interestingly, the sudden increase in the overall replacement rate occurred after a clearly detectable strontianite layer had been formed in the 21 °C experiment at the surface of the celestine crystal (Figure 8),

suggesting an autocatalytical reaction (e.g., [39,40]). As pointed out by Putnis [2], the crystallisation of the solid product phase on the surface of the parent may enhance the dissolution rate of the parent phase, which, in turn, increases the growth rate of the product (termed “autocatalysis”). If true, this could mean that after 6.4 and 14 h, respectively, the precipitation of strontianite has started to catalyse the dissolution of celestine. In this respect, it is noted that the occurrence of an incubation time is a common phenomenon in autocatalysis reactions (e.g., [39]). However, the linear correlation of R^{aq} with the square root of time after 14 h (Figure 9a) indicates that any autocatalysis effect on the dissolution rate had been counterbalanced by the transport of aqueous CO_3^{2-} and SO_4^{2-} through the strontianite surface layer, which became increasingly rate-controlling in the second kinetic regime. Thus, at some point, an ICDP reaction becomes diffusion-controlled, which is also the basic assumption in the shrinking core model [11].

The actual diffusion or better transport properties of the strontianite rim strongly depend on its porosity which, in turn, controls the overall replacement rate [38]. The product phase strontianite has a significantly smaller molar volume ($42.18 \text{ cm}^3/\text{mol}$) than the celestine parent phase ($46.39 \text{ cm}^3/\text{mol}$). The observable porosity in the strontianite product and the formation of a gap at the interface between strontianite and celestine (Figure 5)—where in the framework of the ICDP model, the interface solution is located—can therefore be explained by the difference in the molar volume only. However, the solubility difference of both phases will add up to the porosity given by the molar volume difference [38,41]. Since both phases crystallize in the same orthorhombic crystal structure (space group: *Pmncn*), strontianite will initially topotaxially nucleate onto the celestine surface once its initial dissolution has caused a certain degree of supersaturation in the solution close to the celestine surface. Such topotactic nucleation is energetically favoured compared to any other crystallographic orientation and should result in a polycrystalline, porous strontianite product with crystallographically aligned crystals. The first strontianite layer therefore sets and stabilizes the outer dimension of the pseudomorph. After a continuous strontianite layer has formed, the dissolution of celestine and reprecipitation of strontianite occurs within a thin interface solution film that is connected with the bulk solution via the porosity in the strontianite layer. At this stage, the molar volume and solubility difference between both phases can still be compensated by the formation of porosity in the strontianite layer. However, with increasing thickness of the strontianite layer, the volume change cannot be balanced anymore, and therefore, the thickness of the fluid film at the interface increases. At a certain thickness of the fluid film, new strontianite preferably nucleates onto already existing strontianite rather than onto the celestine surface, as this is energetically favourable. Then, a continuous gap between both phases develops that is clearly visible after the experiments (Figure 5). It is worth noting that such a gap between the parent and product phase has often been observed in nature and in experiments (e.g., [2,3]), but recently, its formation has even directly been observed in operando via fluid-cell Raman spectroscopy [17,19]. However, a fluid film between celestine and strontianite was not observed in the in situ experiment presented here, probably because the strontianite rim was not yet thick enough and the gap was therefore still too small to be detected via Raman spectroscopy, i.e., below about one micrometre.

We observed that at temperatures $\geq 35 \text{ }^\circ\text{C}$, the first kinetic regime, involving the initial celestine dissolution, proceeds so fast that is not recognizable as an individual rate-controlling step. Another intriguing feature of the second kinetic regime is the occurrence of wave-like fluctuations of the R^{aq} and R^s ratio over time around generally linear trends. Small oscillations are also noticeable in the data of the $35 \text{ }^\circ\text{C}$ powder experiment, but not in the data from all other experiments at higher temperatures (Figure 6c). We recall that there is no obvious systematic analytical error that could account for such oscillations. We therefore suggest that the oscillations directly reflect a non-linear coupling of celestine dissolution, strontianite precipitation, and the transport of reactants and products through the strontianite surface layer that only occurs at low temperatures. The transport properties of the strontianite layer therefore controls the chemistry (CO_3^{2-} , SO_4^{2-}) of the interface

solution and thus the celestine dissolution rate that was found to decrease with increasing aqueous SO_4^{2-} [12], i.e., with decreasing chemical affinity. An increase in SO_4^{2-} in the interfacial solution due to transport limitations could thus dramatically decrease the dissolution rate of celestine (chemical affinity approaches zero), while strontianite continues to precipitate, eventually producing self-organized chemical waves. The exact feedback mechanism is not yet understood, but it is noted that temporal chemical oscillations in reacting solutions have also been observed during the dissolution of dolomites and the reprecipitation of a Mg carbonate phase via atomic force microscopy and regular solution sampling [42] and, more recently, during the corrosion of a silicate glass via fluid-cell Raman spectroscopy [20].

Here, we assign the empirical activation energy of 71.8 ± 1.7 kJ/mol, obtained via the time-to-a-given-fraction method from the ≥ 35 °C data at the beginning of the reaction, i.e., far from equilibrium (Figure 7b,c), to the onset of the second kinetic regime of the overall replacement process where the reaction kinetics become ICDP-limited and may be autocatalytical. This value accords well with the apparent activation energies of 64.1 and 70 kJ/mol obtained by fitting shrinking core models to experimental *ex situ* data [10,12]. Using the model of Castillejos et al. [12], however, we obtained a significantly lower apparent activation energy of 22.8 ± 1.7 kJ/mol (Figures 6b and 7a). We nevertheless consider this value to be meaningful because it accords very well with an E_a of 21.6 kJ/mol, reported by Suarez-Orduna et al. [16], and also well with the value of 27.1 ± 0.9 kJ/mol that was obtained in this study via the time-to-a-given-fraction method at infinite conversion progression. Suarez-Orduna et al. [16] obtained a low apparent activation energy from hydrothermal experiments performed between 150 and 250 °C with several millimetre-large single crystal plates. Under such conditions, the initial kinetic steps identified in this study are rate-limiting only in the first minute(s) of the experiments. The measured apparent activation energy therefore likely reflects the final transport-controlled kinetic regime that is established once a certain thickness of the strontianite layer and thus a kind of steady state between transport and celestine dissolution at the ICDP interface has been reached. In this context, it is important to mention that there is evidence that porosity decreases roughly exponentially with an increasing reaction time (so the transport rate within the strontianite layer), slowing the reaction rate [38].

5. Conclusions

The kinetic evaluation of the temporally high-resolution (5 min steps), *in situ* Raman data from the powder experiments at temperatures between 30 and 60 °C showed that the evolution of the solution composition cannot fully be explained by a single rate law derived from the shrinking core model [11] that is basically a simplified mathematical description of the ICDP process. However, by applying the model-independent time-to-a-given-fraction method, we could identify three kinetic regimes with clear changes in the reaction kinetics. The first kinetic regime was not discernible in the data obtained at temperature ≥ 35 °C and involved the stoichiometric dissolution of celestine as the rate-limiting process for which we obtained a high apparent activation energy of 276 ± 11 kJ/mol. Such a high activation energy for the initial surface-controlled kinetic regime has not yet been reported in the literature. The start of the second kinetic regime was characterised by a sudden increase in the conversion rate and was controlled by a non-linear coupling between celestine dissolution, strontianite precipitation, and the transport of aqueous sulphate and carbonate through the growing strontianite surface layer, which also was found to cause chemical oscillations. We obtained an empirical E_a of 71.8 ± 1.7 kJ/mol for this reaction step. The final kinetic regime was clearly transport-controlled with an activation energy of 27.1 ± 0.9 kJ/mol that accorded well with the literature values. It follows that it would cause erroneous predictions of the conversion rate when only the data from temperatures above 30 °C are used to extrapolate the surface temperatures, e.g., to estimate weathering rates.

The results of this study further demonstrate that fluid-cell Raman spectroscopy is a powerful tool to in situ investigate mineral replacement reactions with a micrometre-scale spatial resolution and in case of powder experiments with a high temporal resolution, which allows us to study the reaction steps not detected in ex situ experiments. Short time changes in the kinetics were identified, which were not detected in previous ex situ experimental studies where new samples and solutions had to be used for each time step of an isothermal series. Moreover, the physics behind the Raman effect, i.e., the excitation of the effect via monochromatic light that can be steered through transparent windows, the high spatial resolution, and sensitivity of modern confocal Raman spectrometers along with high information content of a Raman spectrum and the possibility to quantify the oxygen and hydrogen isotope composition of solids and aqueous oxo-anion species [17,43], opens up further avenues to investigate the mechanisms and dynamics of solid–fluid reactions in the future using fluid-cell Raman spectroscopy.

Author Contributions: Conceptualization, M.S. and T.G.; investigation, M.S. and T.G.; methodology, M.S.; supervision, T.G.; visualization and data evaluations, M.S. and T.G.; writing—original draft, M.S. and T.G.; writing—review and editing, M.S. and T.G.; funding acquisition, T.G. All authors have read and agreed to the published version of the manuscript.

Funding: This research was financially supported by the University of Bonn, Germany, and largely via the Deutsche Forschungsgemeinschaft by a grant to T.G. (GE1094/21-1).

Data Availability Statement: The complete data set is available on request from the first author due to internal policy.

Acknowledgments: Many thanks go to Dieter Lülldorf and Henrik Blanchard for building the fluid cells and to three anonymous reviewers whose reviews significantly improved the final manuscript.

Conflicts of Interest: The authors declare no conflicts of interest.

Appendix A

The Raman spectra were collected with a long-working distance (LWD) 100× metallurgical objective (N.A. = 0.8) from a natural celestine crystal that was in contact with pure water. A $170 \pm 5 \mu\text{m}$ thick silicate glass (Schott D 263M) plate was used as a cell window and a lid. A series of x - z scans, with x parallel to the normal of the crystal–water interface and z to the optical (laser) axis, were performed with different confocal hole sizes to obtain an empirical measure of the spatial resolution and the best instrumental settings for the in situ experiments. The extent and morphology of the crystal is best visible in x - z images that are based on color-coding the total intensities in the low-frequency region between 140 and 300 cm^{-1} (Figure A1). In this frequency range, the glass and water give higher but distinguishable intensities (glass boson peak and a water band near 190 cm^{-1}) than the intensity generated from the celestine crystal, producing a clear contrast between all three phases. The Raman image, however, is distorted in the z direction due to the refraction of the laser beam mainly at the air–glass interface, causing an increasing mismatch between the actual distance moved in the z direction by the microscope stage (apparent focal point) and the true focal point. As a consequence, without considering diffraction, the measured thickness of the glass lid would only be $100 \pm 5 \mu\text{m}$ (Figure A1c), i.e., 1.70 ± 0.10 times lower than the expected thickness of $170 \pm 5 \mu\text{m}$. From the Raman images shown in Figure 1b, it is further evident that the confocal hole size not only has a clear effect on the depth, but also on the lateral resolution (note the edge feature that is marked by a red arrow in the images). From the intensity profiles in the x and z directions across the crystal–water interfaces, a lateral, Δx , and an axial resolution, Δz , between about 4 and 5 μm and 16 and 25 μm , respectively, can be determined using the approach illustrated in Figure 1b(C). The true axial resolution, Δz , is therefore about 1.7 times larger (Figure A1c) and strongly depends on the confocal hole size (Figure A1d). At such a depth, the confocal aperture effectively restricts the volume from which a Raman scattering signal is primarily detected (Figure A1d). Taking a confocal hole size of 500 μm at a depth of 180 μm below the glass surface, the Raman

signals were primarily collected from a roughly circular cylindrical volume with a diameter and height of about 4 and 32 μm , respectively. However, the empirically determined lateral resolution is also strongly affected by the non-parallel orientation of the crystal surface with the laser beam axis and/or by the uneven surface morphology (Figure A1a). The small increase in Δx with increasing size of the confocal hole (Figure A1d) may indirectly reflect this misalignment. Therefore, the “true” lateral resolution was likely even better than 4 μm . Accordingly, spatial, chemical or structural variations can principally be much better separated in the x rather than the z direction.

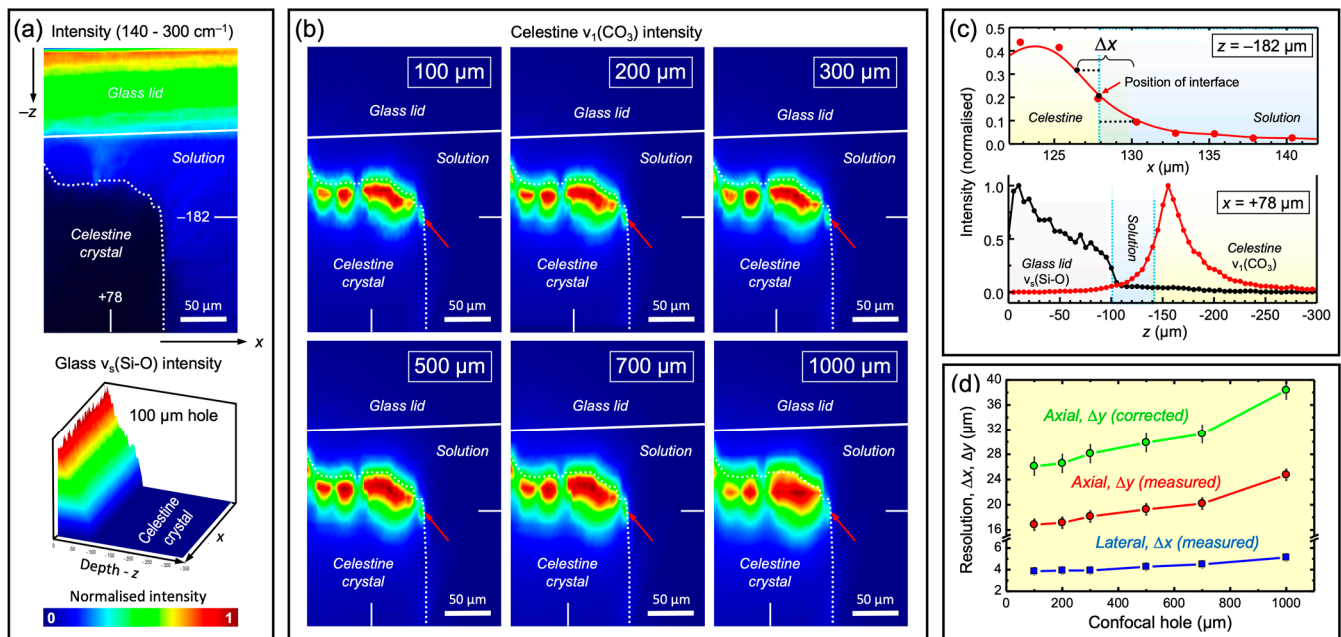


Figure A1. Results of Raman spectroscopic spatial resolution test measurements with a celestine crystal in contact with water. The fluid cell was closed by a glass window as schematically shown in Figure 1b. (a) False-colour x - z image of the total intensity in the frequency region between 140 and 300 cm^{-1} , which give the best visualisation of the morphology of the crystal (stippled white line). Note the $\sim 2^\circ$ mismatch between the laser beam (z) axis and the normal of the glass surface as well as the water layer between glass and crystal. (b) False-colour x - z images of the integrated intensity of the $\nu_1(\text{CO}_3)$ band of celestine obtained with different confocal hole sizes given for each image in the upper right. Note the change in the spatial resolution most pronounced in z direction. This is well recognizable when following the edge feature that is marked by red arrows. (c) Upper diagram: intensity profile of the $\nu_1(\text{CO}_3)$ band intensities of celestine across the celestine–water interface at $z = -182 \mu\text{m}$. Lower diagram: intensity profiles of the $\nu_1(\text{CO}_3)$ band of celestine and the $\nu_s(\text{Si-O})$ bands of the glass window across the glass–water and water–celestine interfaces at $x = 78$. Measurements were made with a confocal hole of 100 μm . As shown in the upper diagram, the position of the interfaces is defined by the point where the intensity reached half of its maximum value. The lateral resolution can be defined as distance between the two points where the intensity reached a quarter and three quarters of its maximum value. From such analysis, one obtains a lateral, Δx , and axial, Δz , resolution of about 4 and 26 μm (corrected for refraction effects). (d) The lateral and axial resolution as a function of confocal hole size.

References

1. Klopogge, J.T.; Lavinsky, R.; Young, S. *Photo Atlas of Mineral Pseudomorphism*; Elsevier: Amsterdam, The Netherlands, 2017; ISBN 978-0-12-803703-4.
2. Putnis, A. Mineral Replacement Reactions: From Macroscopic Observations to Microscopic Mechanisms. *Mineral. Mag.* **2002**, *66*, 689–708. [[CrossRef](#)]
3. Putnis, A. Mineral Replacement Reactions. *Rev. Mineral. Geochem.* **2009**, *70*, 87–124. [[CrossRef](#)]

4. Geisler, T.; Janssen, A.; Scheiter, D.; Stephan, T.; Berndt, J.; Putnis, A. Aqueous Corrosion of Borosilicate Glass under Acidic Conditions: A New Corrosion Mechanism. *J. Non-Cryst. Sol.* **2010**, *356*, 1458–1465. [[CrossRef](#)]
5. Ober, J.A. Strontium in 2015. *Min. Eng.* **2016**, *68*, 30.
6. Singerling, S.A.; Ober, J.A. Strontium. In *Miner Yearbook*; U.S. Geological Survey: Reston, VA, USA, 2015; Volume 73, pp. 1–5.
7. Kobe, K.A.; Deiglmeier, N.J. Strontium Carbonate. *Ind. Eng. Chem.* **1943**, *35*, 323–325. [[CrossRef](#)]
8. Busey, H.S.; Pollard, E.F. Conversion of Strontium Sulfate to Carbonate in Molten State. *Ind. Eng. Chem.* **1948**, *40*, 1988–1990. [[CrossRef](#)]
9. Booth, H.S.; Pollard, E.F. Reactions in Inert Fused Substances: Conversion of Celestine to Strontium Carbonate. *Ind. Eng. Chem.* **1948**, *40*, 1986–1988. [[CrossRef](#)]
10. Iwai, M.; Toguri, J.M. The Leaching of Celestite in Sodium Carbonate Solution. *Hydrometallurgy* **1989**, *22*, 87–100. [[CrossRef](#)]
11. Wen, C.Y. Noncatalytic Heterogeneous Solid-Fluid Reaction Models. *Ind. Eng. Chem.* **1968**, *60*, 34–54. [[CrossRef](#)]
12. Castillejos, A.H.E.; de la Cruz del, F.P.B.; Uribe, A.S. The Direct Conversion of Celestite to Strontium Carbonate in Sodium Carbonate Aqueous Media. *Hydrometallurgy* **1996**, *40*, 207–222. [[CrossRef](#)]
13. Carrillo, F.R.P.; Uribe, A.S.; Castillejos, A.H.E. A Laboratory Study of the Leaching of Celestite in a Pachuca Tank. *Miner. Eng.* **1995**, *8*, 495–509. [[CrossRef](#)]
14. Zoraga, M.; Kahruman, C. Kinetics of Conversion of Celestite to Strontium Carbonate in Solutions Containing Carbonate, Bicarbonate and Ammonium Ions and Dissolved Ammonia. *J. Serb. Chem. Soc.* **2014**, *79*, 345–359. [[CrossRef](#)]
15. Suárez-Orduña, R.; Rendón-Angeles, J.C.; López-Cuevas, J.; Yanagisawa, K. The Conversion of Mineral Celestite to Strontianite under Alkaline Hydrothermal Conditions. *J. Phys. Cond. Mat.* **2004**, *16*, S1331. [[CrossRef](#)]
16. Suárez-Orduña, R.; Rendón-Angeles, J.C.; Yanagisawa, K. Kinetic Study of the Conversion of Mineral Celestite to Strontianite under Alkaline Hydrothermal Conditions. *Inter. J. Min. Process.* **2007**, *83*, 12–18. [[CrossRef](#)]
17. Geisler, T.; Dohmen, L.; Lenting, C.; Fritzsche, M.B.K. Real-Time In Situ Observations of Reaction and Transport Phenomena during Silicate Glass Corrosion by Fluid-Cell Raman Spectroscopy. *Nat. Mater.* **2019**, *18*, 342–348. [[CrossRef](#)] [[PubMed](#)]
18. Lönartz, M.I.; Dohmen, L.; Lenting, C.; Trautmann, C.; Lang, M.; Geisler, T. The Effect of Heavy Ion Irradiation on the Forward Dissolution Rate of Borosilicate Glasses Studied In Situ and Real Time by Fluid-Cell Raman Spectroscopy. *Materials* **2019**, *12*, 1480. [[CrossRef](#)]
19. Lenting, C.; Geisler, T. Corrosion of Ternary Borosilicate Glass in Acidic Solution Studied in Operando by Fluid-Cell Raman Spectroscopy. *NPJ Mater. Degrad.* **2021**, *5*, 37. [[CrossRef](#)]
20. Müller, G.; Fritzsche, M.B.K.; Dohmen, L.; Geisler, T. Feedbacks and Non-Linearity of Silicate Glass Alteration in Hyperalkaline Solution Studied by in Operando Fluid-Cell Raman Spectroscopy. *Geochim. Cosmochim. Acta* **2022**, *329*, 1–21. [[CrossRef](#)]
21. Parkhurst, D.L.; Appelo, C.A.J. Description of Input and Examples for PHREEQC Version 3: A Computer Program for Speciation, Batch-Reaction, One-Dimensional Transport, and Inverse Geochemical Calculations. In *U.S. Geological Survey Techniques and Methods*; U.S. Geological Survey: Reston, VA, USA, 2013; Volume 43, p. 497. [[CrossRef](#)]
22. Rudolph, W.W.; Irmer, G.; Königsberger, E. Speciation Studies in Aqueous HCO_3^- – CO_3^{2-} Solutions. A Combined Raman Spectroscopic and Thermodynamic Study. *Dalton Trans.* **2008**, *7*, 900–908. [[CrossRef](#)]
23. Saloman, E.B.; Sansonetti, C.J. Wavelengths, Energy Level Classifications, and Energy Levels for the Spectrum of Neutral Neon. *J. Phys. Chem. Ref. Data* **2004**, *33*, 1113–1158. [[CrossRef](#)]
24. Hauke, K.; Kehren, J.; Böhme, N.; Zimmer, S.; Geisler, T. In Situ Hyperspectral Raman Imaging: A New Method to Investigate Sintering Processes of Ceramic Material at High-Temperature. *Appl. Sci.* **2019**, *9*, 1310. [[CrossRef](#)]
25. Everall, N.J. Confocal Raman Microscopy: Why the Depth Resolution and Spatial Accuracy Can Be Much Worse Than You Think. *Appl. Spec.* **2000**, *54*, 1515–1520. [[CrossRef](#)]
26. Everall, N.J. Modeling and Measuring the Effect of Refraction on the Depth Resolution of Confocal Raman Microscopy. *Appl. Spec.* **2000**, *54*, 773–782. [[CrossRef](#)]
27. Baldwin, K.J.; Batchelder, D.N. Confocal Raman Microspectroscopy through a Planar Interface. *Appl. Spec.* **2001**, *55*, 517–524. [[CrossRef](#)]
28. Rull, F.; de Saja, J.A. Effect of Electrolyte Concentration on the Raman Spectra of Water in Aqueous Solutions. *J. Raman Spectrosc.* **1986**, *17*, 167–172. [[CrossRef](#)]
29. Lafuente, B.; Downs, R.T.; Yang, H.; Stone, N. The Power of Databases: The RRUFF Project. In *Highlights in Mineralogical Crystallography*; Armbruster, T., Danisi, R.M., Eds.; De Gruyter: Berlin, Germany, 2015; pp. 1–30.
30. Kornicker, W.A.; Presta, P.A.; Paige, C.R.; Johnson, D.M.; Hileman, O.E.; Snodgrass, W.J. The Aqueous Dissolution Kinetics of the Barium/Lead Sulfate Solid Solution Series at 25 and 60 °C. *Geochim. Cosmochim. Acta* **1991**, *55*, 3531–3541. [[CrossRef](#)]
31. Casey, W.H.; Westrich, H.R.; Banfield, J.F.; Ferruzzi, G.; Arnold, G.W. Leaching and Reconstruction at the Surfaces of Dissolving Chain-Silicate Minerals. *Nature* **1993**, *366*, 253–256. [[CrossRef](#)]
32. Hellmann, R. A Leached Layer Hydrolysis Model: A Better Way to Understanding Feldspar Dissolution at Elevated Temperatures and Pressures. *Mineral. Mag. A* **1994**, *58*, 400–401. [[CrossRef](#)]
33. Petit, J.-C.; Mea, G.D.; Dran, J.-C.; Magonthier, M.-C.; Mando, P.A.; Paccagnella, A. Hydrated-Layer Formation during Dissolution of Complex Silicate Glasses and Minerals. *Geochim. Cosmochim. Acta* **1990**, *54*, 1941–1955. [[CrossRef](#)]
34. Putnis, A.; Putnis, C.; Giampaolo, C. The Microtexture of Analcime Phenocrysts in Igneous Rocks. *Eur. J. Mineral.* **1994**, *6*, 627–632. [[CrossRef](#)]

35. Lumpkin, G.R.; Smith, K.L.; Blackford, M.G. Heavy Ion Irradiation Studies of Columbite, Brannerite, and Pyrochlore Structure Types. *J. Nucl. Mater.* **2001**, *289*, 177–187. [[CrossRef](#)]
36. Parker, G.K.; Woods, R.; Hope, G.A. Raman Investigation of Sulfide Leaching. In *Electrochemistry in Mineral and Metal Processing VI: Proceedings of the International Symposium*; Electrochemical Society: Paris, France, 2003; pp. 181–192.
37. Geisler, T.; Nagel, T.; Kilburn, M.R.; Janssen, A.; Icenhower, J.P.; Fonseca, R.O.C.; Grange, M.; Nemchin, A.A. The Mechanism of Borosilicate Glass Corrosion Revisited. *Geochim. Cosmochim. Acta* **2015**, *158*, 112–129. [[CrossRef](#)]
38. Pina, C.M. Topotaxial Replacement of Celestite Single Crystals by Strontianite Aggregates: Pseudomorphisation and Porosity Generation. *Geochim. Cosmochim. Acta* **2019**, *244*, 155–162. [[CrossRef](#)]
39. Anderson, J.G.; Larson, M.A.; Doraiswamy, L.K. Microphase-Assisted “Autocatalysis” in a Solid–Liquid Reaction with a Precipitating Product—II. Experimental. *Chem. Eng. Sci.* **1998**, *53*, 2459–2468. [[CrossRef](#)]
40. Anderson, J.G.; Doraiswamy, L.K.; Larson, M.A. Microphase-Assisted ‘Autocatalysis’ in a Solid–Liquid Reaction with a Precipitating Product—I. Theory. *Chem. Eng. Sci.* **1998**, *53*, 2451–2458. [[CrossRef](#)]
41. Pollok, K.; Putnis, C.V.; Putnis, A. Mineral Replacement Reactions in Solid Solution-Aqueous Solution Systems: Volume Changes, Reactions Paths and End-Points Using the Example of Model Salt Systems. *Am. J. Sci.* **2011**, *311*, 211–236. [[CrossRef](#)]
42. Putnis, A. Why Mineral Interfaces Matter. *Science* **2014**, *343*, 1441–1442. [[CrossRef](#)]
43. King, H.; Geisler, T. Tracing Mineral Reactions Using Confocal Raman Spectroscopy. *Minerals* **2018**, *8*, 158. [[CrossRef](#)]

Disclaimer/Publisher’s Note: The statements, opinions and data contained in all publications are solely those of the individual author(s) and contributor(s) and not of MDPI and/or the editor(s). MDPI and/or the editor(s) disclaim responsibility for any injury to people or property resulting from any ideas, methods, instructions or products referred to in the content.